Classical and ablative Richtmyer-Meshkov instability and other ICF-relevant plasma flows diagnosed with monochromatic x-ray imaging

Y Aglitskiy[1,2], M Karasik[2], A L Velikovich[2], N Metzler[1], S Zalesak[2], A J Schmitt[2], J H Gardner[3], V Serlin[2], J Weaver[2] and S P Obenschain[2]
[1]Science Applications International Corporation, McLean, Virginia 22150
[2]Plasma Physics Division, Naval Research Laboratory, Washington, DC 20375
[3]Berkeley Research Associates, Beltsville, Maryland 20705

E-mail: yefim.aglitskiy@nrl.navy.mil

Abstract. In inertial confinement fusion (ICF) and high-energy density physics (HEDP), the most important manifestations of the hydrodynamic instabilities and other mixing processes involve lateral motion of the accelerated plasmas. In order to understand the experimental observations and to advance the numerical simulation codes to the point of predictive capability, it is critically important to accurately diagnose the motion of the dense plasma mass. The most advanced diagnostic technique recently developed for this purpose is the monochromatic x-ray imaging that combines large field of view with high contrast, high spatial resolution and large throughput, ensuring high temporal resolution at large magnification. Its application made it possible for the experimentalists to observe for the first time important hydrodynamic effects that trigger compressible turbulent mixing in laser targets, such as ablative Richtmyer-Meshkov (RM) instability, feedout, interaction of a RM-unstable interface with rarefaction waves. It also helped to substantially improve the accuracy of diagnosing many other important plasma flows, ranging from laser-produced jets to electromagnetically driven wires in a Z-pinch, and to test various methods suggested for mitigation of the Rayleigh-Taylor instability. We will review the results obtained with the aid of this technique in ICF-HEDP studies at the Naval Research Laboratory and the prospects of its future applications.

PACS numbers: 52.57.Fg, 52.70.La, 52.35.Tc, 47.20.Ma

1. Introduction

Inertial confinement fusion is based on fast compression and heating of spherical deuterium-tritium targets by intense radiation [1-4]. The targets can be imploded either with ultraviolet radiation coming directly from a powerful laser system (direct drive) [3] or with x-rays generated by conversion of laser [2], ion beam or electromagnetic energy [4] into radiation in a hohlraum cavity (indirect drive). In either case, the high-density target shell is accelerated inward by the pressure of the high-temperature lower-density plasma jets ablated from its surface. Similarly to all other situations when a low-density fluid accelerates a high-density fluid, ablative acceleration exhibits the development of Rayleigh-Taylor (RT) instability. Distortion of the ICF target due to the RT and other hydrodynamic instabilities causes mixing of the cold fuel shell material with the hot spot, and thereby can prevent ignition or reduce fusion energy gain in the target. This is why it is one of the critical physics issues of the ICF, see [1-4] and references therein. Mitigation of such hydrodynamic instability is particularly important for the high-gain target designs required for inertial fusion energy. The research program at the Naval Research Laboratory (NRL) seeks to achieve high target performance with direct laser drive by utilizing physics advantages of the krypton-fluoride laser. KrF lasers have deepest UV light, broadest bandwidth and have achieved

the most uniform target illumination of all ICF lasers. The NRL laser-fusion research is aimed at developing the science and technologies for a next-step high-repetition-rate (5 Hz) IFE facility that would require less than 500 kJ of laser energy to produce ~100 MW of fusion thermal power. [5] Our experiments on the 3 kJ Nike KrF laser at NRL [6] seek detailed understanding of laser plasma interactions and the physical processes involved in seeding and growth of the hydrodynamic perturbations that affect the target performance. These results are used to validate and improve the hydrocodes used to simulate spherical implosions thereby increasing confidence in the predictive capability for direct-drive target performance in terms of energy gain and neutron yield.

Evolution of hydrodynamic perturbations in imploding ICF targets is a complicated process. It unfolds over a wide range of spatial and temporal scales, and involves a large variety of hydro instabilities, including RT, Richtmyer-Meshkov (RM), Kelvin-Helmholtz (KH), and combinations thereof, at all stages of their development, ranging from the small-amplitude linear to the weakly and moderately nonlinear regimes to fully developed turbulent mixing. Numerical simulation of this process remains a challenging task even for the state-of-the-art ICF codes. The most advanced modeling is still limited in resolution and relies upon both physical and numerical assumptions and simplifications whose adequacy needs to be constantly tested. For this reason, experimental verification of the codes and validation of the underlying physical models in the ICF-relevant physical conditions has been an area of active study in all the major centers of laser fusion research for the last decades, see [7-15] and references therein.

To obtain experimental data on perturbation growth, which is clean enough to be helpful for testing the codes, one needs adequate diagnostics that combines large field of view with high contrast, high spatial resolution and large throughput, ensuring high temporal resolution at large magnification. Such radiographic diagnostics based on monochromatic x-ray imaging [16] has been advanced in recent years at the Naval Research Laboratory (NRL). It has been first used in our ICF-related hydrodynamic experiments on the NRL's Nike KrF laser [17], and later implemented at other facilities and applied for a variety of ICF/HEDP experiments, e. g., see [18, 19] and references therein.

Our hydrodynamic experiments have been made in planar geometry, in the physical conditions specific for ICF: pressure range ~10 Mbar, time scale ~ 1 ns, spatial scale ~10 μm. We believe, however, that significance of our results extends beyond the immediate practical goal of the ICF code verification. The physical effects that we observe pertain to the basic issues of hydrodynamic instability development and perturbation evolution in shocked and accelerated fluids. Their good understanding is a necessary condition for accurate modeling of the later, more complex stage of perturbation evolution that eventually leads to the turbulent mixing.

This article is structured as follows. In Section 2 we briefly describe monochromatic x-ray imaging diagnostic technique as implemented on Nike. In Section 3 we present some results of our hydrodynamic experiments, which have been made possible by this diagnostics. In section 4 we conclude with a discussion.

2. Diagnostics description

X-ray diagnostics are powerful tools for the study of dense laser-produced plasmas. The surface of these plasmas is hot enough to produce significant quantities of X-radiation for emission spectroscopy. However it is also necessary to diagnose relatively cold and dense portions of targets, to determine their mass nonuniformity. These cold dense plasmas have been diagnosed by absorption of X-rays from external sources [16, 20-27], including X-ray-lasers [28]. Both spectroscopic diagnostics: emission and absorption, similarly require high spectral, spatial, and

temporal resolution. For any backlighting scheme there are two desirable features: smaller size of the backlighter source and filtration of imaging radiation from the self-emission of the object. If the dimension of the source of backlighting radiation is small, the power required to create it can be much smaller than the power driving the object. If spectral filtration is available, the surface brightness of backlighter must be larger than the object brightness only in the bandwidth of the spectral line being used to image the object.

Nike laser has unique capability to generate smooth focal profile with spot size of approximately 0.75 mm FWHM and a 0.4 mm flat top in the center. The large spot size is necessary to minimize the edge effects from the acceleration process and therefore require a diagnostic field of view of approximately 1mm, so that the entire acceleration region as well as the remaining intact part of the target foil are within the picture. A large diagnostic field of view is also required to go with the spot size to obtain good statistics on perturbation evolution.

Monochromatic x-ray imaging system based on Bragg reflection from spherically curved crystals meets all of above mentioned requirements simultaneously [16, 17, 29-37], see figure 1.

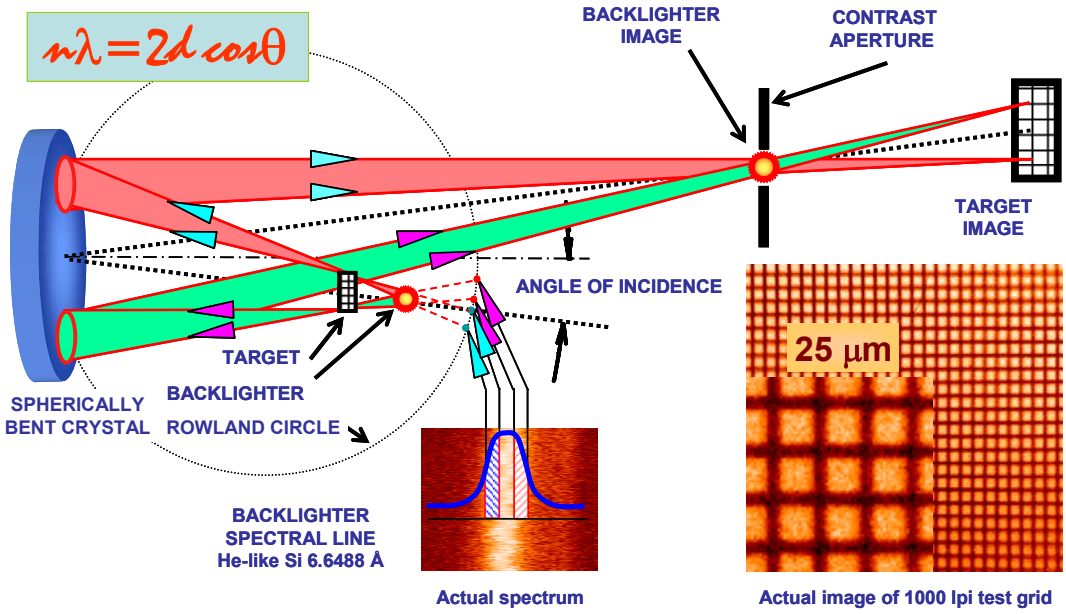

Figure 1. The general scheme of the monochromatic x-ray imaging diagnostics fielded on Nike laser. Also shown: the shape of a Si backlighter spectral line and test images obtained on x-ray film (magnified in the inset).

The energy of 12 Nike beams, ~600 J, is delivered to a silicon backlighter target, producing x-rays that backlight the main target for about 5 ns. A spherically curved quartz crystal selects the resonance line of the He-like Si (1.86 keV, actual spectrum shown in the picture) and projects a monochromatic image of the target on a relevant x-ray detector. For the experiments discussed in this paper, we used a quartz crystal with the cut 1011 and a radius of curvature of 200 or 250 mm. The beams that image the top and the bottom points of test target are shown on Fig.1 to make it clear that our field of view is determined mostly by the crystal size. Test image (with magnified inset) demonstrates good resolution achieved across the large imaging area. In our experiments on Nike and elsewhere we successfully used crystal – spectral line "matching pairs" that cover X-ray energies from 0.6 to 8 keV. In the series of experiments described here we were using 1.86 keV probing energy which was hard enough to study 40 μm to 90 μm thick plastic (CH) targets either flat or rippled with perturbation wavelength λ ranging from 12.5 to 60 μm [38]. Also shown on a

Fig.1 is close-fitting light baffle with an aperture stop just larger than the size of the backlighter image that has been placed in the reflected beam to block most of the continuum radiation from the plastic target. It provides an effective spectral and spatial filtering of the monochromatic imaging radiation from the unwanted broad-band self-emission of the target.

At NRL, a curved crystal imager has been used at first in combination with a framing camera to provide sequences of high spatial resolution still images taken with a time resolution of 200 ps [34]. However, measurements of mass perturbation evolution due to Richtmyer-Meshkov (RM) instability (ripples on the front surface) or feedout (ripples on the back side) related oscillations present new challenge to imaging diagnostics because of essentially non-monotonic evolution of the processes under study [8-10]. To extend the capabilities of our diagnostic technique we added a streak camera to the system, which made it possible to analyze continuous time behavior of an x-ray image. High throughput of the x-ray optical system allowed us to magnify the images by a factor of 10-20 to compensate for the modest resolution of framing and streak cameras.

Spherically bent crystal can provide: 1D spatially resolved x-ray spectra, monochromatic images of the laser plasma blowoff, etc. [17], but in our recent experiments we were particularly interested in the measurements of areal mass variation in rippled and flat plastic targets ablatively accelerated by the Nike laser. The setup provides spatial resolution in one relevant direction, i.e. along the wave vector of the ripple on the target surface, producing 1D streak records [8-10].

The streak records were taken with a time resolution of 170 ps. This is sufficient for the 0.5 ns characteristic times of interest. The large field of view (500 μm) combined with the large flat top (400 μm) of the laser focal spot gave us more ripples available for Fourier transform analysis, thus ensuring confidence in determining the dominant mode amplitude. It also allowed us to use more complicated targets incorporating simultaneously two different characteristics (wavelengths, thicknesses, amplitudes etc.) thus making comparative analysis independent from shot-to-shot variations and therefore more reliable.

3. Direct observation of hydrodynamic perturbation evolution in laser targets

Most of the studies of hydrodynamic perturbation evolution in laser targets concentrated on the ablative RT instability [7, 11-15], which amplifies plasma non-uniformities by orders of magnitude and contributes most to the target distortion. Due to the limited dynamic range of the diagnostics perturbations become observable as they reach large amplitudes. They are not visible during the earlier stages as they are seeded. “RT seeding” is the process of formation of the exponentially growing RT eigenmodes from target imperfections, small-scale laser imprint, and large scale irradiation non-uniformity due to beam pointing errors and imbalance. The seeding process that starts from very small perturbation amplitudes is notoriously difficult to model numerically. Early-time perturbation growth can be artificially suppressed with numerical diffusion or drowned in a numerically generated noise, which may result, respectively, in over-optimistic or over-pessimistic numerical predictions of the target performance [39]. Until very recently, little experimental data were available for testing the codes in the RT-seeding relevant regimes. The situation changed with the development of new diagnostic techniques [8-11, 40]. Some examples are presented below in this section.

3.1. Classical Richtmyer-Meshkov instability in finite-thickness targets

Classical RM instability [41] develops when a planar shock wave interacts with a rippled contact interface between two different materials. The small-amplitude theory predicts an asymptotically linear growth of the interfacial ripple amplitude and of the areal mass modulation amplitude for each mode. Typically, classical RM growth proceeds in the positive or negative direction (interfacial ripples deepen with time, either maintaining their initial phase, or having the phase

reversed) if the incident shock wave arrives to the interface from a lighter or a heavier fluid side, respectively. The wave reflected from the interface is a shock wave in the former case and a rarefaction wave in the latter; the transmitted wave is always a shock. The interfacial growth slows down but continues in the nonlinear regime as the spikes acquire the characteristic mushroom shapes (for details, see [42, 43] and references therein).

Classical RM growth has been studied on major ICF glass laser facilities, NOVA and OMEGA [44]. In these experiments, special care was taken to ensure that the measurements were made before any of the shock and/or rarefaction waves propagating from the shocked interface through both unperturbed materials could reach any other contact surfaces or interfaces, thereby sending shock or sonic waves back to the RM unstable interface. This is, of course, a necessary condition of isolating the effect of RM instability growth. However, this effect is not really isolated when such growth at an internal interface in a laser target contributes to the RT seeding. The target starts accelerating only after the hydrostatic equilibrium in it has been established by a passage of all shock and rarefaction waves back and forth. Interaction of such waves with an internal interface determines the contribution of classical RM growth at this interface to the RT seeding.

Our experiments [10] were made with planar targets that featured a single-mode, two-dimensional (2D) rippled interface separating low-density resorcinol formaldehyde foam from solid plastic. Typical parameters of our targets were: foam density $\rho_1 = (0.2-0.3)\times\rho_2$, where $\rho_2 = 1.07$ g/cm^3 is the density of solid plastic; ~130 μm thick foam layer, ~20 μm thick plastic layer, ripple wavelength $\lambda = 30$ μm and amplitude $\delta x_0 = 2.5$ μm. The targets could be irradiated from either side, triggering light-to-heavy or heavy-to-light classical RM instability at the plastic-foam interface. They were driven by a 4-ns long Nike laser pulse, with or without a ~5%, 3 ns foot.

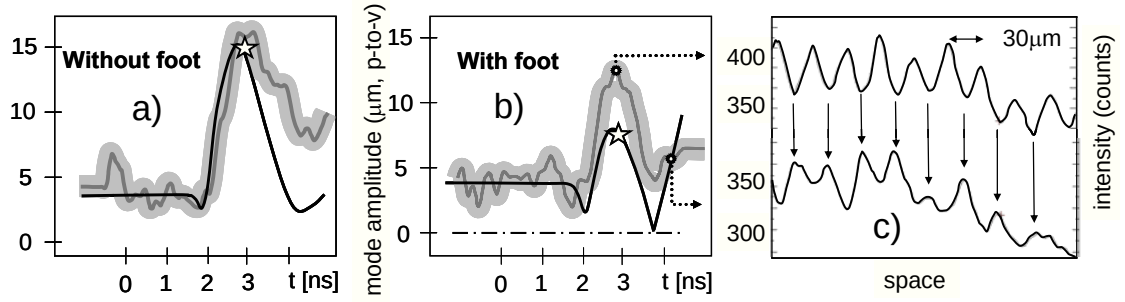

Figure 2. Simulated (black) and measured (gray lines) amplitudes of the dominant Fourier mode for a target irradiated from the foam side by Nike pulses without (a) and with foot (b). Stars in (a), (b) indicate the onset of acceleration. (c) Lineouts of the streak records at 3 and 4 ns showing a phase reversal of areal mass modulation. The thickness of the shaded area approximately corresponds to the experimental uncertainty of the Fourier amplitude measurement near zero.

Figure 2 demonstrates the results obtained in the light-to-heavy shots, when the laser irradiated the targets from the low-density foam side. Here and below $t = 0$ corresponds to the half-rise of the main pulse, and the mode amplitude shown is the absolute value of the peak-to-valley areal mass modulation amplitude, $|\delta m(t)|$ for the dominant Fourier mode divided by ρ_2. When the shock wave, having passed through the foam layer, reaches the foam-CH interface, it starts the classical RM growth in the positive direction. However, when the acceleration starts, the RT growth is seen to proceed in the opposite direction, thereby reducing the areal mass modulation amplitude. This occurs for the Nike pulses without and with foot, illustrated by figures 2(a) and 2(b), respectively. Our simulations predicted a phase reversal of δm before the end of the main

pulse with a foot: $\delta m(t)$ passes through zero and, as long as the laser pulse is on, continues to grow in the negative direction, accumulating more mass where there was less of it initially. Figure 2(c), showing the lineouts of the streak records taken at the moments $t = 3$ and 4 ns indicated by small circles on figure 2(b), demonstrates that this is indeed the case: Valleys of the areal mass are observed at 4 ns at exactly the same places where the peaks were at 3 ns.

This behavior, observed for the first time in [10], is explained by the interaction of the classically RM-unstable interface with a rarefaction wave that arrives from the rear side of the solid CH layer after the shock breakout. When it arrives to the interface, the lower-density foam is decompressed earlier because of its higher speed of sound. The lateral pressure gradient will then be directed from the foam bubbles to the CH spikes, thereby driving the spikes of heavy fluid into the bubbles of light fluid and changing the direction of variation of δm. Inertia of this motion shapes the areal mass perturbation profile, which is later exponentially amplified by the RT instability. When the laser pulse has a foot, as in figure 2(b), the foam is pre-compressed by the foot, hence the classical RM growth phase becomes shorter, the interaction of the RM-unstable foam-CH interface with the reflected rarefaction wave occurs earlier, so that the lateral mass flow triggered by it continues long enough to invert the phase of δm and drive the RT growth with the inverted phase.

Figure 3 illustrates the case when our target is irradiated from the high-density plastic side, a heavy-to-light classical RM instability, as in [44]. In a classical case, the amplitude $\delta m(t)$ is predicted to rapidly change phase and grow in the negative direction, as observed in [44] and discussed in detail in [43, 45]. Such behavior is not seen in figure 3, which happens to be quite similar to figure 2. This is because the observed time histories of δm are not dominated by either case of the classical RM instability but rather by the interaction of the secondary rarefaction and/or shock waves arriving from the ablation front and the rear surface of the target to the foam-CH interface.

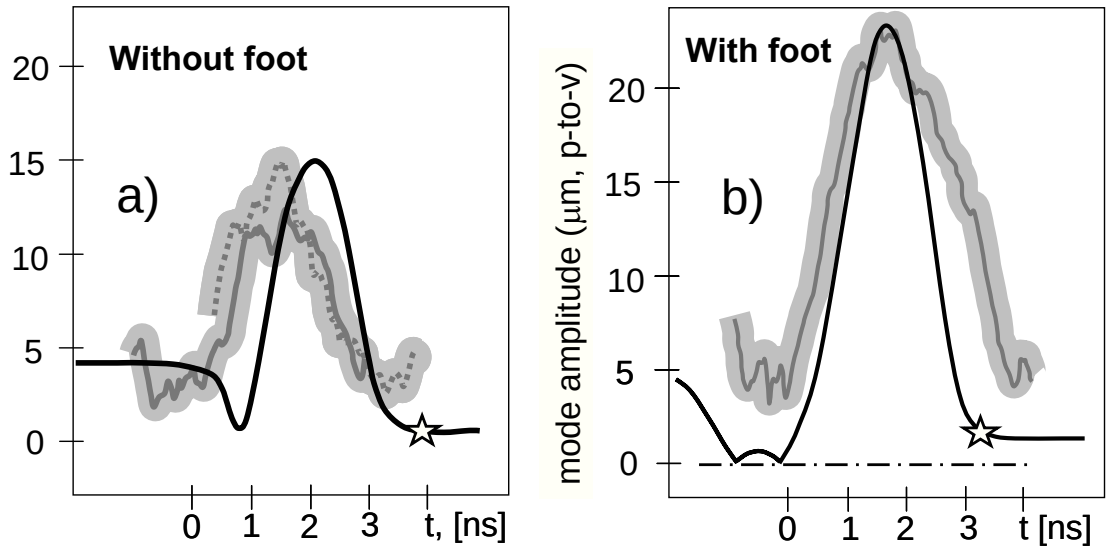

Figure 3. Simulated (black) and measured (gray lines) amplitudes of the dominant Fourier mode for a target irradiated from the plastic side by Nike pulses without (a) and with foot (b). Stars indicate the onset of acceleration. Gray solid and dashed lineouts represent two shots taken consequently in order to cover whole laser pulse without foot. The thickness of the shaded area

approximately corresponds to the experimental uncertainty of the Fourier amplitude measurement near zero.

The time available for the classical RM growth in conditions of figure 3 is very short, about 0.2 ns, because of the small thickness of the shock-compressed plastic layer. When the rarefaction wave reflected from the CH-foam interface reaches the ablation front, where a higher pressure is maintained, a so-called adjustment shock is reflected from it, propagating through the high-density CH back to the RM unstable interface. Re-shock of this interface reverses the direction of the perturbation growth, from negative to positive. This growth in the positive direction continues until the adjustment shock catches up the transmitted shock front in the foam and a rarefaction wave reflected from it comes back to the interface, once again reversing the direction of variation of δm as described above. For a laser pulse with a foot, the incident shock wave in plastic is slower, there is more time available for the classical heavy-to-light RM growth in the negative direction, and larger amplitude of interfacial modulation is reached by the time when the interface is re-shocked. Since the shock wave transmitted into the foam is also slower, the interval between the re-shock and the arrival of the rarefaction wave reflected from the rear surface to the material interface is longer, allowing more time for the RM growth in the positive direction after the re-shock. Therefore the peak of $|\delta m|$ is predicted to be higher for the pulse with a foot, in contrast with the situation of figure 2 when the target is irradiated from the low-density foam side. Experimental data of figure 3 demonstrate that this is indeed the case: a higher peak is observed for the Nike pulse with a foot. Ablation front starts accelerating shortly before the end of the pulse, hence no time is left for the RT growth. Indeed, no late-time phase reversal is observed for either case, as predicted by the simulations.

3.2. Ablative Richtmyer-Meshkov instability

Ablative RM instability is the physical mechanism responsible for the RT-seeding triggered by the roughness of the irradiated target surface. When the laser radiation hits the target, it launches a shock wave propagation into the target from the ablation front. If the instantly turned on laser radiation flux is constant, which is a realistic assumption for a foot of the pulse in direct-drive ICF [3], then the ablation front instantly acquires a constant velocity. In a sense, this is a shock-piston problem, where a constant ablative pressure applied to the target surface acts as a piston driving the shock wave into the target.

Having instantly applied a high constant external pressure to a half-space bounded by a rippled surface, we would trigger the development of a RM-type hydrodynamic instability [46] at this surface. Although it is not exactly the same as the classical light-to-heavy RM instability, it develops in pretty much the same way. In particular, unlimited perturbation growth, linear with time, is predicted for the small-amplitude regime. A similar behavior during the shock transit time was expected for a laser target with a rough surface being irradiated by a constant, uniform laser beam, instantly turned on.

Surprisingly, simulations performed for small initial amplitudes of the single-mode ripples on the irradiated surface of the target [47] did not confirm linear growth. Rather, they revealed slowly decaying oscillations of the ablation front ripple amplitude, as well as of δm. The theory of this effect was given in [48], where the term “ablative RM instability” was coined. It is different from the classical RM instability because the ablation front that serves as a piston is very different from a free surface or a material interface. Recall that the classical RM instability is driven mainly by the vorticity deposited in the fluid particles at the interface during the shock passage [43]. Plasma particles do not stay at the ablation front; rather, they flow through it to the low-density corona, dissipating the initially deposited vorticity. Moreover, the perturbed ablation front exhibits a

restoring force similar to a surface tension. It emerges because the ablation front, as first shown in [49], is an isotherm. When it is perturbed, and a part of it gets closer to the hot corona, the temperature at the ablation front does not increase, but the temperature gradient in its vicinity, ∇T, does. This in turn increases the local heat flux to the ablation front, $-\kappa\nabla T$, and hence the rate of mass ablation [50], thereby increasing the ablative pressure and pushing this part of the ablation front back. The physics of this "rocket effect" is explained in detail in [48, 50]. Dissipation and restoring force, both due to mass ablation, make the difference between classical and ablative RM instability. Instead of the linear growth characteristic of classical RM case, the ablation front ripples and δm exhibit decaying oscillations [47, 48]. Frequency of these oscillations is estimated as $\Omega_a \cong k v_a / r_D^{1/2}$, where $k = 2\pi/\lambda$ is the ripple wavenumber, v_a is the ablation velocity, $r_D << 1$ is the effective blowoff-plasma-to-ablation front density ratio. For $v_a \cong 10^5$ cm/s, which is characteristic for plastic targets irradiated by Nike beams at 50 TW/cm^2, $\lambda = 30$ μm and $r_D \cong 0.07$, we find that the half period of the oscillation is ~4 ns, about the same as duration of the Nike pulse.

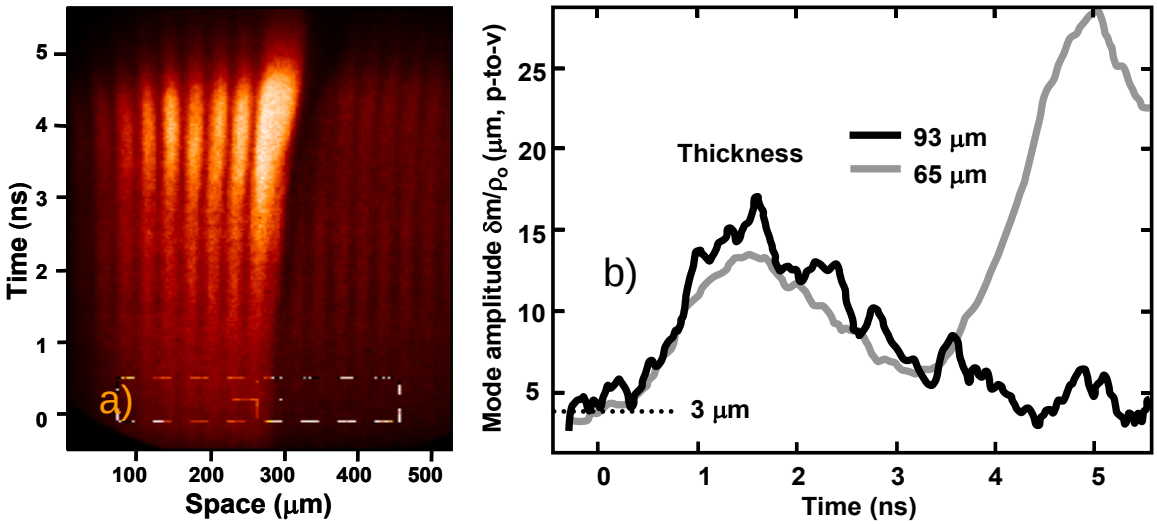

Figure 4. (a) Streak record of the stepped target rippled on the front side. (b) Amplitudes of the dominant Fourier mode vs. time for a 93 μm (black) and 65 μm thick (gray) parts of the target; horizontal dotted line shows the initial peak-to-valley amplitude.

We reported the first direct observation of the areal mass oscillations due to ablative Richtmyer-Meshkov instability in [8]. Here it is illustrated with figure 4. The streak image shown in figure 4(a) has been obtained for a stepped target whose planar front surface has been rippled ($\lambda = 45$ μm and peak-to-valley ripple amplitude 3 μm). The backlighted left half of the target is brighter than its right half because it is thinner: Their thicknesses are, respectively, 65 μm and 93 μm. Since the two halves of the target are driven by the same laser pulse, the stepped target design ensures that the ablative RM oscillation proceeds identically in both during the shock transit time. The transit time, however, is shorter for the thinner left half of the target. It starts accelerating earlier than the thicker right half, thereby ending the oscillation and switching to the ablative RT growth while in the right half the ablative RM oscillation continues till the end of the Nike pulse. This is illustrated by figure 4(b) showing the time histories of peak-to-valley amplitudes of the dominant Fourier mode for thin and thick areas of the target, normalized as in figures 2, 3. Within the experimental error, which is larger for the thicker half because of higher attenuation, their evolution up to $t = 3.5$ ns is identical. The early phases of the oscillation are clearly seen: the

amplitude increases, reaches its peak and starts to decrease. The oscillation in the thinner half is terminated by the arrival of the rarefaction wave from the rear surface of the target to the ablation front, starting the onset of acceleration at about $t = 2.5$ ns. Shortly after this, the onset of the ablative RT growth in the positive direction is observed. In the thicker right half of the target, the oscillation continues. It has been shown that it is thick enough to achieve the phase reversal of the areal mass modulation amplitude occurring shortly before the end of the laser pulse [10].

3.3. Feedout

Feedout is the physical mechanism responsible for the RT-seeding triggered by the roughness of the rear target surface [45, 51-53]. The RT growth begins after a shock wave initiated at the smooth irradiated surface of the target breaks out at its rippled inner (or rear, in planar geometry) surface, and a rippled rarefaction wave reflected from it reaches the front surface. The shock rarefaction transit time is shorter for the thinner parts of the target, which start accelerating earlier. If the wavelength of the rear-surface ripples is long enough compared to the shock compressed target thickness, $kL_s << 1$, then the thinner parts of the target also experience a higher acceleration under the same driving pressure because of their lower areal mass. As a result, these thinner parts evolve into bubbles, propagating ahead and dumping more of their mass into the spikes that trail behind, as predicted in [51] and observed in [52].

If the ripple wavelength is shorter than the initial thickness of the target, then the lateral mass redistribution in the reflected rippled rarefaction wave cannot be neglected. When a shock wave first breaks out at the valleys of the rippled rear surface, expansion and decompression start from there, whereas the pressure in the shock front still propagating towards the peaks remains at constant post-shock value. The resulting lateral pressure gradient starts driving mass from peaks to valleys (note the similarity with the situation illustrated in figure 2), decreasing the pressure near the peaks and increasing it near the valleys, at some point overshooting the equilibrium and building up a reverse pressure gradient. The oscillations of the areal mass in a rippled rarefaction wave have been described in detail in [45, 54]. Early phases of such oscillations have been detected in the indirect-drive feedout experiments of [53].

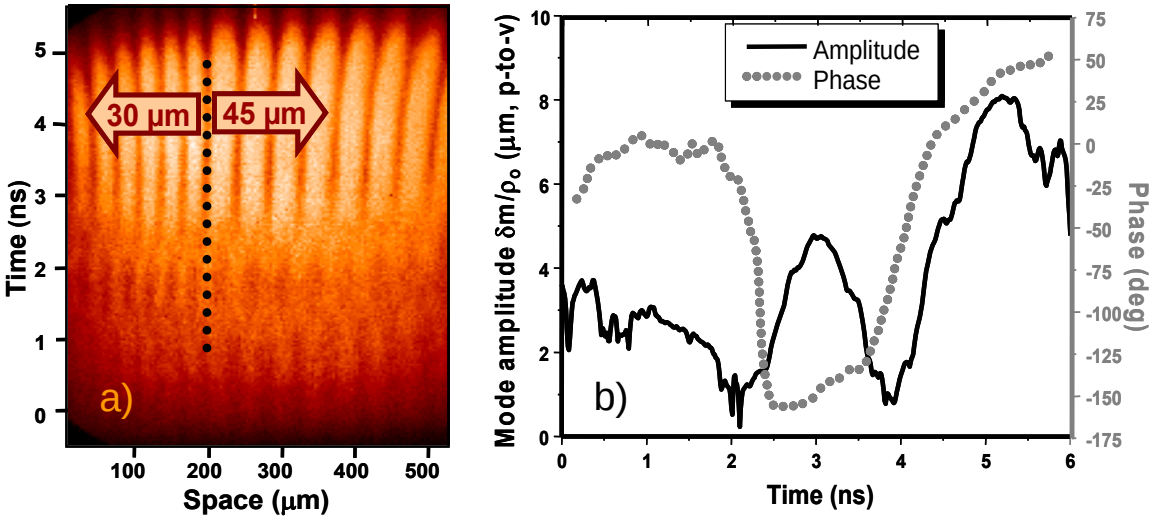

Figure 5. (a) Streak record of a target rippled on the rear side with two wavelengths: 30 μm and 45 μm. (b) Amplitude (black) and phase (gray) of the dominant Fourier mode vs. time for the 45 μm wavelength.

In [9, 10] we reported the first direct observation of the whole evolution of perturbation caused by feedout in a planar target: areal mass oscillation in a rippled rarefaction wave, two phase reversals and a subsequent RT growth. Figure 5(a) shows the streak record obtained for a 60 μm thick target rippled on the rear side: the ripple wavelength is 30 μm and 45 μm for its left and right half, respectively. The light and dark stripes indicating, respectively, low and high areal mass, are seen at early time, then they disappear. Then the stripes reappear, but the light and dark ones change places, indicating a phase reversal, similar to that shown in figure 2(b, c). Shortly after this, the RT growth of δm in the positive direction begins, and the phase of δm is reversed again. Figure 5(b) shows the time histories of the peak-to-valley amplitude and phase of the dominant Fourier mode, normalized as above, for the left, short-wavelength half of the target. The two phase reversals are clearly observed.

3.4. Foil collisions

Experiments on collisions of planar foils have been pioneered at NRL and carried out since the early days of laser fusion [55]. The x-ray burst observed at collision of the laser-accelerated foil (the impactor) with a stationary, "witness" foil, or impactee, made it possible to measure the velocity of the impactor and to evaluate the uniformity of its velocity profile [55]. In later experiments [56] it was demonstrated that the density gradient scale length of the impactor could be determined from observations of double- and triple-foil collisions.

The advanced x-ray radiographic diagnostics described in Section 2 opened new possibilities for colliding-foil experiments. Using face-on and side-on radiographic diagnostics simultaneously, one can directly determine the impactor velocity, evaluate the impactor mass, infer the mass ablation rate, measure the target non-uniformity, both in flight and after the collision, at the acceleration phase. Therefore the colliding foil experiments bring valuable information about the impactor and open a new area of well-diagnosed high-energy density hydrodynamic experiments in the pressure range between tens and hundreds of Mbar.

The importance of such experiment stems from the fact that hydrodynamic instability growth in a plasma shell which is rapidly decelerated is an important feature of all scenarios of laser fusion ignition [1-3]. A dense shell, either directly or indirectly imploded, drives a shock wave into a low-density DT fuel inside it. After collapse of this shock at the center of the target, the reflected expanding shock wave hits the imploding shell, impulsively starting its deceleration. Similar processes of rapid deceleration from an ultra-high velocity play a prominent role in recently suggested innovative approaches to direct-drive ignition, such as impact ignition and shock ignition. Impact ignition [57] relies upon heating of a semi-spherical ignitor DT shell accelerated to a hyper-velocity ~1000 km/s at collision with a resting dense compressed fuel. Shock ignition [58] involves fast re-compression of an expanding central hot spot with a converging shock wave driven by a short, powerful "ignitor spike" laser pulse irradiating the target at peak compression. Both concepts [57] and [58] involve a dynamic formation of a contact interface bounding the heated DT plasma. In impact ignition [57], an interface between the ignitor plasma and the cold DT fuel is dynamically formed in the impact. Below we describe the experiments focused on the RM-type and ablative RT perturbation growth triggered and/or affected by foil collisions.

The ubiquitous non-uniformities of the colliding plasmas are imprinted at collision into the dynamically formed interface and trigger a vorticity-driven hydrodynamic instability growth in its vicinity. This growth can drive mixing and generate the seeds for subsequent RT growth. A dynamically formed material interface emerges at collision of foils and is shocked at the same time. It was demonstrated in [46] that a hydrodynamic instability similar to the classical RM instability must develop on non-uniform interfaces. This effect is referred to as the RM-like [46]

or RM-type instability. It had been predicted theoretically and confirmed in numerical simulations but never observed experimentally before our first direct observations.

Our targets consisted of a smooth planar plastic ~20 μm thick "impactor" foil separated by a ~80 μm vacuum space from a "impactee" foil, which is ~30 μm thick and rippled from the front side facing the other foil (λ = 30 to 45 μm, peak-to-valley amplitude 3 to 10 μm). The Nike laser beams drive the smooth impactor foil, producing its head-on collision with the rippled impactee foil. Before collision, little perturbation growth of the dominant mode is expected because the ripples remain essentially unperturbed until the impact (in some situations, the x-ray radiation coming from the impactor foil can affect the early evolution of the ripples). After collision, a rippled interface is shaped, and two shock waves start propagating from it into the impactor and impactee foils. We deal here with the RM-type growth in a finite-thickness target, which is physically similar to the case of classical RM growth described above in section 3.1.

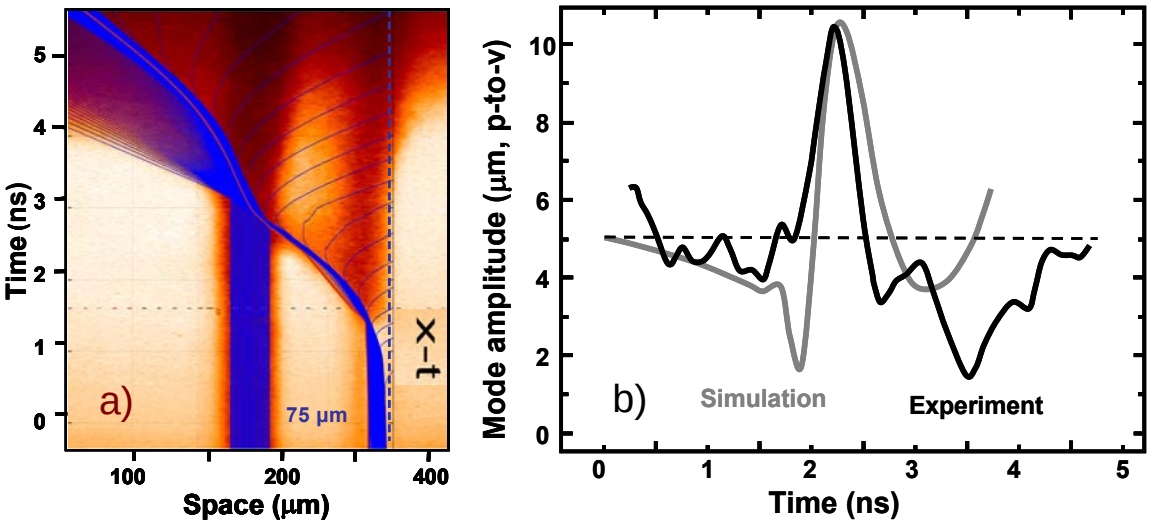

Figure 6. (a) Streak record of the side-lighted double-foil target with rippled front side of the rear foil. Blue lines are *x*-*t* trajectories of plasma particles from 1-D simulations. (b) Amplitude of the dominant Fourier mode vs. time for the 30 μm wavelength: experiment (black) and 2-D simulation (gray).

Our typical results are presented in figure 6. The time history of collision is illustrated by figure 6(a), where the original streak record of the side-lighted double-foil target is overlaid with a *x*-*t* diagram obtained in a 1D simulation (blue lines are Lagrangian trajectories of fluid particles). The time history of the dominant Fourier mode is shown in figure 6(b), where the results of 2D simulation are also plotted. The rapid RM-type growth is seen to stop and reverse its direction after the rarefaction wave comes from the ablation front, in the same way as it happens when a classical RM instability is developed in finite-thickness targets, see section 3.1 above. This growth pattern has been found to be very robust and reproducible. Note its similarity with the growth shown in figure 2.

We have also performed experiments with a rippled plastic foil hitting a planar foam foil. If the laser drive continues through the impact, the ablation front gets re-shocked by a shock wave coming from the target. Such a re-shock is a feature of the shock ignition scenario [58], which seeks to heat the central hot spot area by a strong shock from a laser spike after the compression shock wave has reflected from the center of the target, when its vicinity starts expanding. We

observed the same rate of the RT growth in a double-foil target as in a single target until the impact. Shortly after that, the RT growth is seen to stop and reverse its direction. This reversal of the growth direction is apparently due to the arrival of the reflected shock wave from the impact to the ablation front. It triggers the mass flow in the negative direction in a very similar way to the feedout case of section 3.3. Pressure in the reflected shock wave is higher than that maintained by the laser at the ablation front. Therefore the reflected shock wave produces a decompression - a secondary reflected rarefaction wave - as it breaks out at the ablation front. The valleys of the rippled ablation front get decompressed first, while the reflected shock wave still propagates through the peaks, maintaining a higher post-shock pressure there.

3.5. Multi-mode evolution measurements

The curved crystal imaging technique is not limited to single mode perturbation growth. High resolution, throughput, and large field of view allow observation of pre-imposed as well as stochastic (e.g., laser imprint) perturbations. An example of this is shown in figure 7a, which shows time evolution of areal mass perturbations on a CH foil with a pre-imposed 0.5 μm peak-to-valley amplitude, 60 μm and 30 μm wavelength sinusoidal ripple [59]. The pre-imposed surface perturbation is not seen on the streak record of figure 7(a) initially due to its small starting amplitude, but it gradually becomes visible as it grows. As seen on the spatial spectrum plot of figure 7(b), the RT growth of the initially pure 60 μm mode of the front surface ripple is accompanied by broadband growth seeded by the non-uniformity of the laser radiation - laser imprint. By approximately 2 ns, the perturbation is no longer purely sinusoidal. However, the 30 μm second harmonic of the initial ripple expected at this non-linear growth stage is coupled with imprint and does not appear as a distinct mode in the spectrum. For a case of a 30 μm wavelength initial ripple, the pre-imposed perturbation grows faster and dominates the evolution even into the non-linear stage, as seen in a spectrum in figure 7(c). It remains a well-defined mode, with its 15 μm harmonic clearly distinct from the noise background.

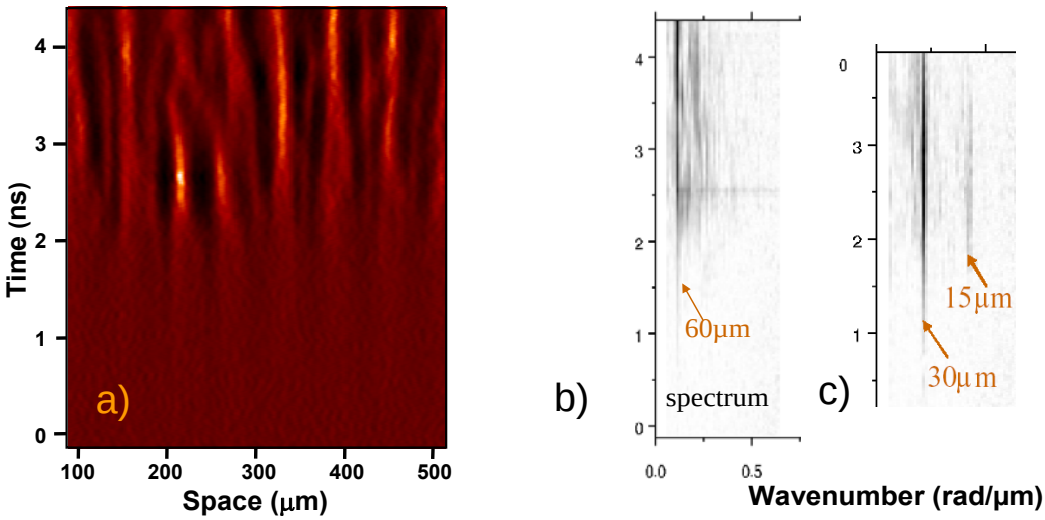

Figure 7. Non-linear interaction of pre-imposed ripple and laser imprint: (a) streak image for $\lambda = 60$ μm; (b) time history of the areal mass Fourier spectrum for $\lambda = 60$ μm; (c), spectrum for $\lambda = 30$ μm.

3.6. Cryogenic target evolution

The technique is applicable to cryogenic targets as well as room temperature ones. Figure 8 shows the RT perturbation growth on a smooth 0.1 g/cm^3 resorcinol-formaldehyde (RF) foam

wicked with cryogenic hydrogen [60]. Such a foil is a planar mock-up of the ablator of a high-gain ICF target design, in which the foam allows increased laser absorption as well as easier pellet fabrication. Radiography x-rays are absorbed by the foam, giving the perturbation evolution history. There is no pre-imposed modulation here, so the observed broadband perturbation growth is seeded entirely by laser imprint.

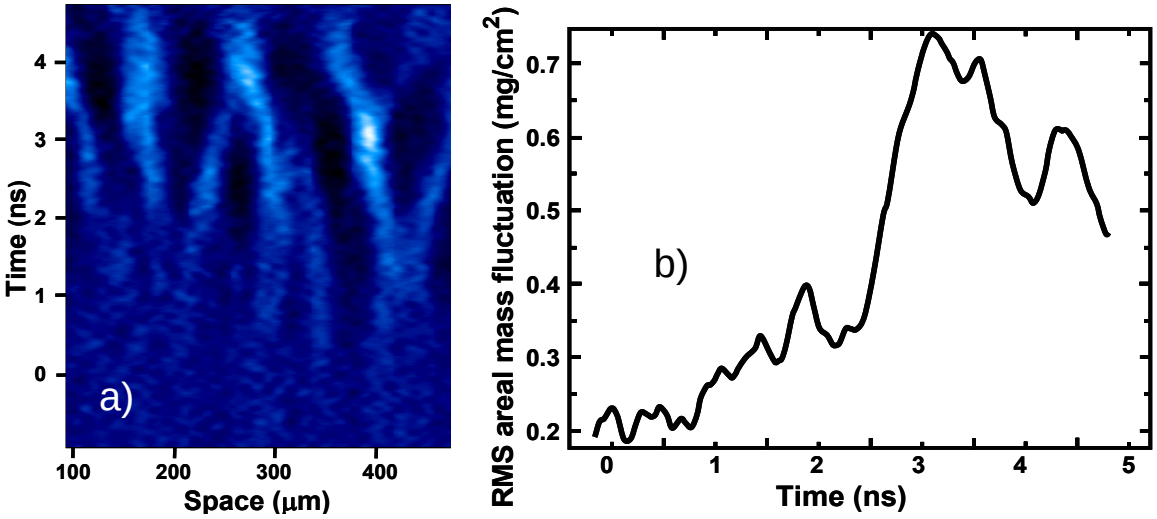

Figure 8. Laser imprint on cryogenic hydrogen-wicked foam: (a) streak image; (b) time history of the rms areal mass fluctuation.

3.7. Testing the efficiency of the instability mitigation techniques

Mitigation of the hydro instabilities of the implosion, primarily of the ablative RT instability of the target acceleration, is one of the most important directions of the ICF studies. The degree of the RT perturbation growth can make all the difference between the ignition/high-gain implosion and a fizzle.

The main parameter affecting both the ablative RM perturbation seeding and the ablative RT perturbation growth is the mass ablation velocity, $v_a = \dot{m}/\rho_a$, where $\dot{m}$ is the rate of mass ablation and ρ_a is the plasma density at the ablation front. Therefore, the most effective way of the instability mitigation is increasing the ablation velocity v_a while maintaining the ablative pressure essentially the same. It has been shown [61] that v_a scales as $1/\rho_a$. Therefore one can increase v_a by tailoring the density profile in the target, with density at the ablation front reduced as much as possible. Having defined the target adiabat as $\alpha = p_a / p_F$, where p_a is the pressure at the ablation front and $p_F \propto \rho^{5/3}$ is the pressure of the Fermi gas for the given electron density, we see that $v_a \propto \alpha^{3/5}$, hence the effective instability mitigation is achieved by the large adiabat tailoring. The outer layers of the target should be kept at high adiabat, to produce large v_a, whereas its inner part should be kept at low adiabat, to make its high compression possible – for details, see [62].

An effective method of softening the target's outer layers uses a short burst of x-ray radiation. For this, the target is covered by a very thin (~1000 Å) layer of a high-Z material, like gold or palladium [63]. Laser radiation absorbed by the high-Z material is immediately converted into x-

rays and re-radiated, ablating the target by x-ray drive until the high-Z layer expands and becomes transparent.

Mitigation of the instability growth seeded by front surface roughness is clearly illustrated by figure 9. It presents the results of an experiment made with a 60 μm thick target rippled on the front side (λ = 30 μm, peak-to-valley amplitude 3 μm). The right half of the target is uncoated plastic and the left half is coated with a 800 Å layer of Pd. The initial amplitude of the ripples is the same, but their growth is seen to be more pronounced in the right, pure CH half of the target. This is confirmed with figure 7(b) comparing the time histories of the areal mass modulation amplitude for the dominant Fourier mode for the two halves.

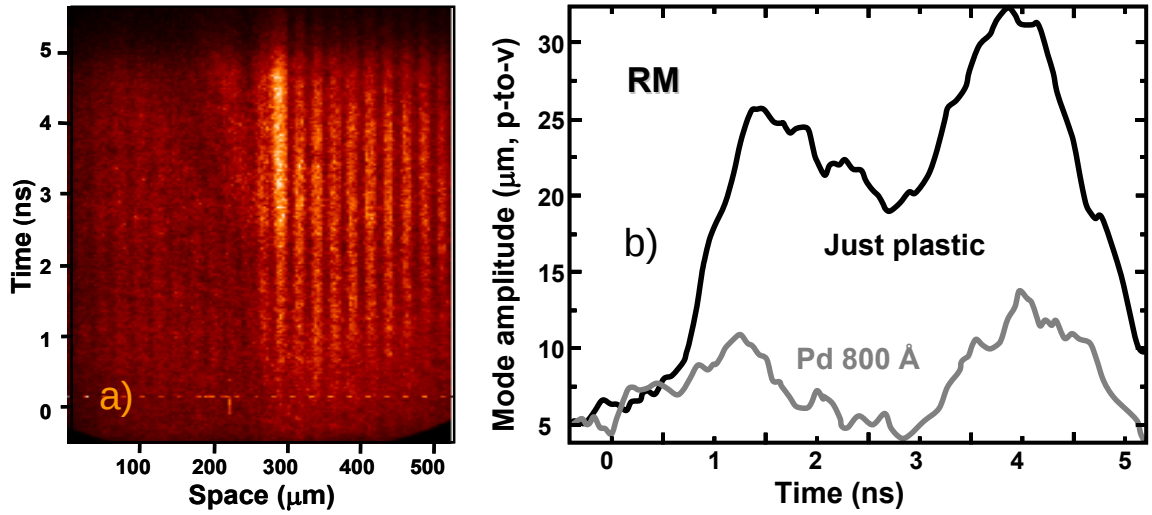

Figure 9. (a) Streak record of the half-coated target rippled on the front side. (b) Amplitude of the dominant Fourier mode vs. time for the uncoated (black) and coated (gray) parts of the target.

For the pure plastic, the perturbation evolution presented in figure 7(b), is very similar to that shown in Fig. 4(b). It starts as ablative RM oscillation occurring during the shock transit time. Shortly after the start of acceleration, at about 2.7 ns, the ablative RT instability takes over. Essentially the same is seen to occur in figure 7(b), but the amplitude of the ablative RM oscillations is seen to be strongly suppressed due to increased ablation velocity. Since the areal mass of the Pd coating is small, the shock transit time is the same for both halves of the target, and the ablative RT growth starts simultaneously. In the coated half of the target, however, it starts from lower initial amplitude, thereby demonstrating an efficient suppression of the RT seeding with the high-Z coating.

4. Conclusions

Monochromatic x-ray imaging diagnostics is a powerful tool for observing dynamics of ICF targets and probing the lateral mass redistribution due to hydro instabilities, waves and other transient processes. The available experimental results obtained with the aid of this diagnostics constitute a valuable, extensive data base for benchmarking hydrocodes and testing theoretical models.

The examples presented in Section 3 above demonstrate that mass ablation, shock loading, radiation of high-Z layers, finite dimensions of targets, interaction of shock and rarefaction waves with stable and unstable surfaces and interfaces and other ICF/HEDP specific phenomena play

important role in seeding and growth of hydrodynamic instabilities and mixing. The well-known hydrodynamic instabilities, such as RT, RM or KH (not discussed here but also studied in recent experiments on Nike), attain new features and develop differently in ICF/HEDP relevant situations. Accurate modeling of their growth, from the early-time, small-amplitude regime through nonlinear phase to the turbulent mixing stage still remains a challenging task. Much needs to be done in the theory, simulation and experiment in order to achieve confidence in our predictive capability for direct-drive target performance. The development of such capability is one of the most important steps to the inertial fusion energy.

Acknowledgments

We are grateful to Dr. S. I. Abarzhi for her suggestion to present this review at the international conference “Turbulent mixing and beyond” and to participants of this conference for valuable discussion. We thank Nike Laser Crew for their excellent technical support. This work was supported by the U. S. Department of Energy, Defense Programs.

References

[1] Atzeni S and Meyer-ter-Vehn J 2004 *The Physics of Inertial Fusion. Beam Plasma Interaction, Hydrodynamics, Hot Dense Matter* (Oxford: Oxford University Press)

[2] Lindl J D 1998 *Inertial Confinement Fusion: the Quest for Ignition and Energy Gain Using Indirect Drive* (New York: AIP Press – Springer)

[3] Bodner S E, Colombant D G, Gardner J H, Lehmberg R H, Obenschain S P, Phillips L, Schmitt A J, Sethian J D, McCrory R L, Seka W, Verdon C P, Knauer J P, Afeyan B B, and Powell H T1998 *Phys. Plasmas* **5** 1901

[4] Matzen M K, Sweeney M A, Adams R G, Asay J R, Bailey J E, Bennett G R, Bliss D E, Bloomquist D D, Brunner T , Campbell R B, Chandler G A, Coverdale C A, Cuneo M E, Davis J P, Deeney C, Desjarlais M P, Donovan G L, Garasi C J, Haill T A, Hall C A, Hanson D L, Hurst M J, Jones B, Knudson M D, Leeper R J, Lemke R W, Mazarakis M G, McDaniel D H, Mehlhorn T A, Nash T J, Olson C L, Porter J L, Rambo P K, Rosenthal S E, Rochau G A, Ruggles L E, Ruiz C L, Sanford T W L, Seamen J F, Sinars D B, Slutz S A, Smith I C, Struve K W, Stygar W A, Vesey R A, Weinbrecht E A, Wenger D F, and Yu E P 2005 *Phys. Plasmas* **12** 055503

[5] Obenschain S P, Colombant D G, Schmitt A J, Sethian J D, and McGeoch M W 2006 *Phys. Plasmas* **13** 056320

[6] Obenschain S P, Bodner S E, Colombant D, Gerber K, Lehmberg R H, McLean E A, Mostovych A N, Pronko M S, Pawley C J, Schmitt A J, Sethian J D, Serlin V, Stamper J A, Sullivan C A, Dahlburg J P, Gardner J H, Chan Y, Deniz A V, Hardgrove J, Lehecka T, Klapisch Mand 1996 *Phys. Plasmas* **3** 2098

[7] Grun J, Emery M H, Kacenjar S, Opal C B, McLean E A, Obenschain S P, Ripin B H, and Schmitt A 1984 *Phys. Rev. Lett.* **53** 1352
Grun J, Emery M H, Manka C K, Lee T N, McLean E A, Mostovych A, Stamper J, Bodner S, Obenschain S P, and Ripin B H 1987 *Phys. Rev. Lett.* **58** 2672
Pawley C J, Bodner S E, Dahlburg J P, Obenschain S P, Schmitt A J, Sethian J D, Sullivan C A, Gardner J H, Aglitskiy Y, Chan Y, and Lehecka T 1999 *Phys. Plasmas* **6** 565

[8] Aglitskiy Y, Velikovich A L, Karasik M, Serlin V, Pawley C J, Schmitt A J, Obenschain S P, Mostovych A N, Gardner J H, and Metzler N 2001 *Phys. Rev. Lett.* **87** 265001

[9] Aglitskiy Y, Velikovich A L, Karasik M, Serlin V, Pawley C J, Schmitt A J, Obenschain S P, Mostovych A N, Gardner J H, and Metzler N 2001 *Phys. Rev. Lett.* **87** 265002

[8] Aglitskiy Y, Velikovich A L, Karasik M, Serlin V, Pawley C J, Schmitt A J, Obenschain S P, Mostovych A N, Gardner J H, and Metzler N 2002 *Phys. Plasmas*. **9** 2264

[10] Aglitskiy Y, Metzler N, Karasik M, Serlin V, Velikovich A L, Obenschain S P, Mostovych A N, Schmitt A J, Weaver J, Gardner J H, and Walsh T 2006, *Phys. Plasmas*. **13**, 080703

[11] Desselberger M, Willi O, Savage M, and Lamb M J 1990 *Phys. Rev. Lett.* **65** 2997
Desselberger M and Willi O 1993, *Phys. Fluids* B **5** 896

[12] Azechi H, Nakai M, Shigemori K, Miyanaga N, Shiraga H, Nishimura H, Honda M, Ishizaki R, Wouchuk JG, Takabe H, Nishihara K, Mima K, Nishiguchi A, and Endo T 1997 *Phys. Plasmas.* **11** 4079
Shigemori K, Azechi H, Nakai M, Honda M, Meguro K, Miyanaga N, Takabe H, and Mima K 1997 *Phys. Rev. Lett.* **78** 250
Azechi H, Sakaiya T, Fujioka S, Tamari Y, Otani K, Shigemori K, Nakai M, Shiraga H, Miyanaga N, and Mima K 2007 *Phys. Rev. Lett.* **98** 045002

[14] Remington B A, Haan S W, Glendenning S G, Kilkenny J D, Munro D H, and Wallace R J 1992 *Phys. Fluids* B **4** 967
Remington B A, Weber S V, Marinak M M, Haan S W, Glendenning S G, Kilkenny J D, Wallace R J, and Dimonte G 1994 *Phys. Rev. Lett.* **73** 545.
Remington B A, Weber S V, Marinak M M, Haan S W, Glendenning S G, Kilkenny J D, Wallace R J, and Dimonte G 1995 *Phys. Plasmas* **2** 241

[15] Knauer J P, Betti R, Bradley D K, Boehly T R, Collins T J B, Goncharov V N, McKenty P W, Meyerhofer D D, Smalyuk V A, Verdon C P, Glendinning S G, Kalantar D H, and Watt RG 2000 *Phys. Plasmas* **7** 338

[16] Rode A V, Maksimchuk A M, Sklizkov G V, Ridgley A, Danson C, Rizvi N, Bann R, Forster E, and Uschmann I 1990 *Opt. Commun.* **7** 163
Pikuz S A, Shelkovenko T A, Romanova V M, Hammer D A, Faenov A Ya, Dyakin V A, and Pikuz T A 1997 *Rev. Sci. Instrum.* **68** 740

[17] Aglitskiy Y, Lehecka T, Obenschain S, Bodner S, Pawley C, Gerber K, Sethian J, Brown C M, Seeley J, Feldman U, and Holland G 1998 *Appl. Opt.* **37** 5253 (1998).
Aglitskiy Y, Lehecka T, Obenschain S, Bodner S, Pawley C, Brown C M, Seeley J, Feldman U and Holland G 1998 *Rev. Sci. Instrum.* **70** 530
Sethian J D, Bodner S E, Colombant D G, Dahlburg J P, Obenschain S P, Pawley C J, Serlin V, Gardner J H, Aglitskiy Y, Chan Y, Deniz A V, Lehecka T, and Klapisch M 1999 *Phys. Plasmas* **6** 2089

[18] Sinars D B, Bennett G R, Wenger D F, Cuneo M E, Hanson D L, Porter J L, Adams R G, Rambo P K, Rovang D C, and Smith I C 2004 *Rev. Sci. Instrum.* **75** 3672

[19] Loupias B, Falize E, Koenig M, Bouquet S, Ozaki N, Benuzzi-Mounaix A, Michaut C, Rabec le Goahec M, Nazarov W, Courtois C, Aglitskiy Y, Faenov A Ya and Pikuz T 2007 *Astrophys Space Sci.* **307** 103

[20] Whitlock R, Obenschain S P and Grun J 1982 *Appl. Phys. Lett.* **41** 429

[21] Fraenkel B S 1982 *Appl. Phys. Lett.* **41** 234

[22] Lewis C L S and McGlinchey J 1985 *Opt. Comm.* **53** 179

[23] Whitlock R R, Obenschain S P, Grun J, Stamper J A, Sprague J A, Sweeney B V, Ripin B H, and Craxton R S 1987 *J. Appl. Phys.* **61** 131

[24] Balmer J, Lewis C L S, Corbett R E, Robertson E, Saadat S, O'Neill D, Kilkenny J D, Back C A, and Lee R W 1989 *Phys. Rev.* A **40**, 330

[25] Davidson S J, Neely D, Lewis C L S, and O'Neil D 1991 "Sub-keV x-ray point projection absorption measurements," *Rutheford Appleton Laboratory Annual Report* **RAL-91-025**

[26] Perry T S, Davidson S J, Serduke F J, Bach D. R, Smith C C, Foster J M, Doyas R J, Ward R A, Iglesias C A, Rogers F J, Abdallah Jr J, Stewart R E, Kilkenny J D, and Lee R W 1991 *Phys. Rev. Lett.* **67** 3784

[27] Da Silva L B, Barbee Jr T W, Cauble R, Celliers P, Harder J, Lee H R, London R A, Mathews D L, Mrowka S, Moreno J C, Ress D, Trebes J E, Wan A and Weber F 1995 *Rev. Sci. Instrum.* **66** 574

[28] Da Silva L B, Barbee Jr T W, Jr., Cauble R, Celliers P, Ciarlo D, Libby S, London R A, Mathews D, Mrowka S, Moreno J C, Ress D, Trebes J E, Wan A S, and Weber F 1995 *Phys. Rev. Lett.* **74** 3991

[29] Pikuz S A, Shelkovenko T A, Romanova V M, Hammer D A, Faenov A Ya, Dyakin V A, and Pikuz T A 1995 *JETP Lett.* **61**, 638

[30] Pikuz S A, Shelkovenko T A, Romanova V M, Hammer D A, Faenov A Ya, Dyakin V, and Pikuz T A 1995 in *Soft X-Ray Lasers and Applications*, Rocca J J and Hagelstein P L, ed., Pros. SPIE **2520** 330

[31] Pikuz T A, Faenov A Ya, Pikuz S A, Romanova V M, and Shelkovenko T A 1995 *Journal of X-ray Science and Technology* **5** 323
[32] Aglitskiy Y, Lehecka T, Deniz A, Hardgrove J, Seely J, Brown C, Feldman U, Pawley C, Gerber K, Bodner S, Obenschain S, Lehmberg R, McLean E, Pronko M, Sethian J, Schmitt A, Sullivan C, Holland G and Laming M 1996 *Phys. Plasmas* **3** 3438
[33] Brown C, Seely J, Feldman U, Obenschain S, Bodner S, Pawely C, Gerber K, Serlin V, Sethian J, Aglitskiy Y, Lehecka T, and Holland G 1997 *Rev. Sci. Instrum*. **68** 1099
[34] Brown C, Seely J, Feldman U, Obenschain S, Bodner S, Pawley C, Gerber K, Sethian J, Mostovich A, Aglitskiy Y, Lehecka T, and Holland G 1997 *Phys. Plasmas* **4** 1397
[35] Sanchez del Rio M, Faenov A Ya, Dyakin V A, Pikuz T A, Pikuz S A, Romanova V M, and Shelkovenko T A 1997 Physica Scripta , **55**, 735-740 (1997).
[36] Pawley C J, Gerber K, Lehmberg R H, McLean E A, Mostovych A N, Obenschain S P, Sethian J D, Serlin V, Stamper J A, Sullivan C A, Bodner S E, Colombant D, Dahlburg J P, Schmitt A J, Gardner J H, Brown CSeely J F, Lehecka T, Aglitskiy Y, Deniz A V, Chan Y, Metzler N, and Klapisch M 1997 Phys. Plasmas **4** 1969
[37] Pikuz S A, Shelkovenko T A, Romanova V M, Hammer D A, Faenov A Ya, Dyakin V A, and Pikuz T A 1997 *Rev. Sci. Instr*. **68** 740
[38] Pawley C J, Bodner S E, Dahlburg J P, Obenschain S P, Schmitt A J, Sethian J D, Sullivan C A, Gardner J H, Aglitskiy Y, Chan Y, and Lehecka T, Observation of Rayleigh-Taylor growth to short wavelengths on Nike 1999 *Phys. Plasmas* **6** 565
[39] Zalesak S T, Schmitt A J, Gardner J H and Velikovich A L 2005 *Phys. Plasmas* **12** 056311
[40] Gotchev O V, Goncharov V N, Knauer J P, Boehly T R, Collins T J B, Epstein R, Jaanimagi PA, and Meyerhofer D D 2006 *Phys. Rev. Lett*. **96** 115005
[41] Richtmyer RD 1960 *Commun. Pure Appl. Math.* **13** 297
Meshkov EE 1969 *Fluid Dyn.* **4**(5) 101
[42] Holmes R L, Dimonte G, Fryxell B, Gittings M L, Grove J W, Schneider M, Sharp D H, Weaver R P, Velikovich A L, and Zhang Q 1999 *J. Fluid Mech.* **389** 55
[43] Wouchuk J G 2001 *Phys. Rev*. E **63** 056303
Wouchuk J G 2001 *Phys. Plasmas* **8** 2890
[44] Dimonte G and Remington B 1993 *Phys. Rev. Lett*. **70** 1806
Glendinning S G, Bolstad J, Braun D G, Edwards M J, Hsing W W, Lasinski B F, Louis H, Miles A, Moreno J, Peyser T A, Remington B A, Robey H F, Turano E J, Verdon C P, and Zhou Y 2003 *Phys. Plasmas* **10** 1931
[45] Velikovich A L, Schmitt A J, Gardner J H, and Metzler N 2001 *Phys. Plasmas* **8** 592
[46] Velikovich A L, Dahlburg J P, Schmitt A J, Gardner J H, Phillips L, Cochran F L, Chong Y K, Dimonte G, and Metzler N 2000 *Phys. Plasmas* **7** 1662
[47] Velikovich A L, Dahlburg J P, Gardner J H, and Taylor R J 1998 *Phys. Plasmas* **5** 1491
[48] Goncharov V N 1999 *Phys. Rev. Lett*. **82** 2091
[49] Bodner S E 1974 *Phys. Rev. Lett*. **33** 761
[50] Sanz J 1994 *Phys. Rev. Lett*. **73** 2700
Piriz A R, Sanz J and Ibañez L F 1997 *Phys. Plasmas* **4** 1117
[51] Betti R, Lobatchev V, and McCrory R L 1998 *Phys. Rev. Lett*. **81** 5560
[52] Shigemori K, Nakai M, Azechi H, Nishihara K, Ishizaki R, Nagaya T, Nagatomo H, and Mima K 2000 *Phys. Rev. Lett.* **84** 5331
[53] Smitherman D P, Chrien R E, Hiffman N M, and Magelssen G R 1999 *Phys. Plasmas* **6** 932
[54] Velikovich A L, Zalesak S T, Metzler N and Wouchuk J G 2005 *Phys. Rev*. E **72** 046306
[55] Obenschain S P, Grun J, Ripin B H, and Mclean E A 1981 *Phys. Rev. Lett*. **46** 1402
Grun J, Obenschain S P, Ripin B H, Whitlock R R, Mclean E A, Gardner J, Herbst M J, and Stamper J A 1983 *Phys. Fluids* **26** 588
[56] Bolotin V A, Gavrilov V V, Golberg S M, Goltsov A Y, Kondrashov V N, Kovalsky N G, Velikovich A L, and Zavyalets S V 1992 *Phys. Fluids* B **4** 2596
[57] Murakami M, Nagatomo H, Azechi H, Ogando F, Perlado M, and Eliezer S 2006 Nucl Fusion **46** 99
[58] Betti R, Zhou C D, Anderson K S, Perkins L J, Theobald W, and Solodov A A 2007 *Phys. Rev. Lett*. **98** 155001
[59] Karasik M, Aglitskiy A, Serlin V, and Bates J W, 2005 Bull. Am. Phys. Soc. **50**(8) 58

[60] Karasik M, Weaver J L, Aglitskiy Y, Mostovych A N, Serlin V, Bates J W, Gardner J H, and Obenschain S P 2004 34th Anomalous Absorption Conference, Gleneden Beach, Oregon, May 2004 4P2
[61] Mora P 1982 *Phys. Fluids* **25** 1051
Manheimer W M, Colombant D G, and Gardner J H 1982 *Phys. Fluids* **25** 1644
[62] Goncharov V N, Knauer J P, McKenty P W, Radha P B, Sangster T C, Skupsky S, Betti R, McCrory R L, and Meyerhofer D D 2003 *Phys. Plasmas* **10** 1906
[63] Obenschain S P, Colombant D G, Karasik M, Pawley C J, Serlin V, Schmitt A J, Weaver J L, Gardner J H, Phillips L, Aglitskiy Y, Chan Y, Dahlburg J P, and Klapisch M 2002 *Phys. Plasmas* **9** 2234